Π-Electron-Extended Porphyrin-Linked Covalent Organic Framework for a Q-Switched All-Solid-State Laser

Kuan-Ying Chen, Hsuan-Sen Wang, Shih-Po Su, Shiao-Wei Kuo,* Chao-Kuei Lee,* and Ahmed F. M. EL-Mahdy*

Herein, a new π-electron-delocalized building block (ProPh-4CHO) is reported for the construction of a π-electron-extended porphyrin/pyrene-linked covalent organic framework (ProPh-PyTA-COF) for use as a saturable absorber (SA) in a Q-switched all-solid-state laser. Employing a mode-locked fiber laser operated with 130-fs pulses at 1030 nm and a repetition rate of 28 MHz, ProPh-PyTA-COF exhibits remarkable optical nonlinear absorptions: two saturable absorptions with saturation intensities of 92 MW cm^{-2} and 1 kW cm^{-2}. This material is used to fabricate the first pulsed Q-switched all-solid-state laser incorporating a COF as an absorber. The laser incorporating this COF-SA exhibited a pump power of 6.5 W with a pulse duration of 1.2 μs, corresponding to a pulse repetition rate of 94.4 kHz. This study not only reveals the possibility of using saturation absorption to pulse a solid-state laser but also opens up a new path toward optical nonlinearity through the engineering of π-bond delocalization.

1. Introduction

Laser technology has been a major field in physics and photonics since its first demonstration in the 1960s.[1] Among the various types of lasers, passive Q-switching and mode-locking have become essential techniques for generating giant laser pulses with pulse widths ranging from microseconds to femtoseconds.[2] In addition to the cavity design, the saturable absorber (SA) plays key role in starting and stabilizing the pulsed operation.[3] In the 1990s, with successes in semiconductor fabrication, semiconductor saturable absorber mirrors (SESAMs) replaced

conventional absorbers (e.g., Cr:YAG) as the most popular way for pulsing lasers.[4] Despite the advantage of self-starting, a limited operation wavelength range decreased their utility. As a result, a challenge remains to develop new material systems and devices. Several parameters are considered critical for optimizing the pulse operation, including a rapid relaxation time and broadband operation. Using graphene as the SA, Zhang et al. reported a mode-locked fiber laser.[5] Thereafter, many material systems, including topological insulators (TIs),[6] black phosphorus (BP),[7] transition metal dichalcogenides (TMDs)[8] and Mxene,[9] were developed for pulsing lasers, for both fiber lasers and solid-state lasers operating over various wavelengths ranging from the visible to the mid-infrared. The capability for the broadband operation has attracted much attention in the past decade. An SA functions with the rule that it absorbs light at low intensity but becomes transparent at high intensity. In addition, the saturation intensity and modulation depth also influence the performance of the pulsed laser. For example, a lower saturation intensity and a higher modulation depth have been realized as guidelines for optimization. Accordingly, tunability of the optical nonlinearity of a SA is a required feature.

Compared with conventional inorganic SAs, metal–organic frameworks (MOFs) appear to have greater capability for use in optical nonlinear engineering, because their inherent band structure and electronic features can be controlled rationally through structural modification.[10] In addition, their use in adaptive, inexpensive, and flexible device fabrication has attracted tremendous attention. As an alternative to MOFs, covalent organic frameworks (COFs) have been proposed to enhance optical nonlinearity through the effects of their π-electrons.[11,12] COFs are ordered, crystalline, low-density, porous materials that feature the atomically exquisite integration of building units into extended 2D and 3D periodic structures.[13–19] Traditionally, COFs have been designed by forming covalent bonds among, typically, C, N, S, Si, O, and B atoms through reversible condensation.[20–22] Because of their outstanding persistent porosities, electrochemical activities, chemical/thermal stabilities, and π-stacked architectures, COFs have a range of applications in, for example, adsorption/storage, semiconductors, the removal of pollutants from wastewater, conversion electronics,

K.-Y. Chen, S.-W. Kuo, A. F. M. EL-Mahdy
Department of Materials and Optoelectronic Science
National Sun Yat-Sen University
Kaohsiung 80424, Taiwan
E-mail: kuosw@faculty.nsysu.edu.tw; ahmedelmahdy@mail.nsysu.edu.tw

H.-S. Wang, S.-P. Su, C.-K. Lee
Department of Photonics
National Sun Yat-Sen University
Kaohsiung 80424, Taiwan
E-mail: chuckcklee@yahoo.com

catalysis, and photoenergy.[23–35] The ability to engineer the structures of conjugated organic building blocks allows the construction of new COFs, with such molecules connected and stacked to generate periodical π-columnar architectures. This approach has resulted in the discovery of a number of new organic COF semiconductors with regular π-skeletons.[36–40] Upon the polycondensation of such semiconductors, several COFs have been developed as potential platforms for photoelectronic applications.[41–43]

Among the many available π-extended molecules, porphyrins possess excellent thermochemical stabilities, the ability to incorporate a wide variety of metals, and diverse electrochemical and optical properties; as a result, they have attracted considerable interest for use in organic field effect transistors, organic photovoltaic cells, and organic light emitting diodes.[44–49] Nevertheless, there remains a desire to enhance the optical and electronic properties of porphyrins. For example, extending the π-electron delocalization in porphyrins can be achieved through the incorporation of additional aromatic rings into the main skeleton or through polycondensation and coupling with other porphyrin units or large moieties with delocalized π-electrons (e.g., pyrene and biphenyl).[50–55] Along this line, in this study we developed a π-electron-extended porphyrin/ pyrene-linked COF as a novel system for use in a Q-switched solid-state laser; to the best of our knowledge, no such applications have been reported previously. Herein, we discuss the construction of this new large π-electron-delocalized building block, the development of the novel π-electron-extended porphyrin/pyrene-linked COF, and its distinct characteristics within a Q-switched all-solid-state laser.

2. Results and Discussion

2.1. COF Design, Synthesis, and Characteristics

We used the Suzuki–Miyaura reaction to synthesize the new π-electron-extended building block ProPh-4CHO (Scheme S1, Supporting Information). The palladium-catalyzed coupling of 5,10,15,20-tetrakis(4-bromophenyl)porphyrin (Por-4Br, Figure S1–S3, Supporting Information) with 4-formylphenylboronic acid in the presence of potassium carbonate as the base, performed in a mixture of 1,4-dioxane and water (1:0.2, v/v) at 100 °C, produced the desired ProPh-4CHO building block in high yield. In its Fourier transform infrared (FTIR) spectrum, ProPh-4CHO provided signals at 1700, 1603, and 1471 cm^{-1} corresponding to aldehydic C=O and aromatic C=C stretching vibrations, as well as a set of signals in the range from 2847 to 2796 cm^{-1}, attributable to the aldehydic H—C=O stretching vibration (**Figure 1**b). Nuclear magnetic resonance (NMR) spectroscopy confirmed the chemical structure of ProPh-4CHO. The ^{1}H NMR spectrum of ProPh-4CHO featured a sharp singlet at 10.15 ppm, representing the four aldehydic CHO groups, as well as signals for aromatic C—H groups in the range from 8.86 to 8.03 ppm (Figure S4, Supporting Information). In the ^{13}C NMR spectrum of ProPh-4CHO, the signal for the aldehydic C=O carbon nuclei appeared at 192.93 ppm (Figure S5, Supporting Information).

Figure 1a presents our strategy for the synthesis of the novel π-electron-extended porphyrin/pyrene-linked COF (ProPh-PyTA-COF) from the new ProPh-4CHO building block. Briefly, we synthesized the ProPh-PyTA-COF solvothermally through the
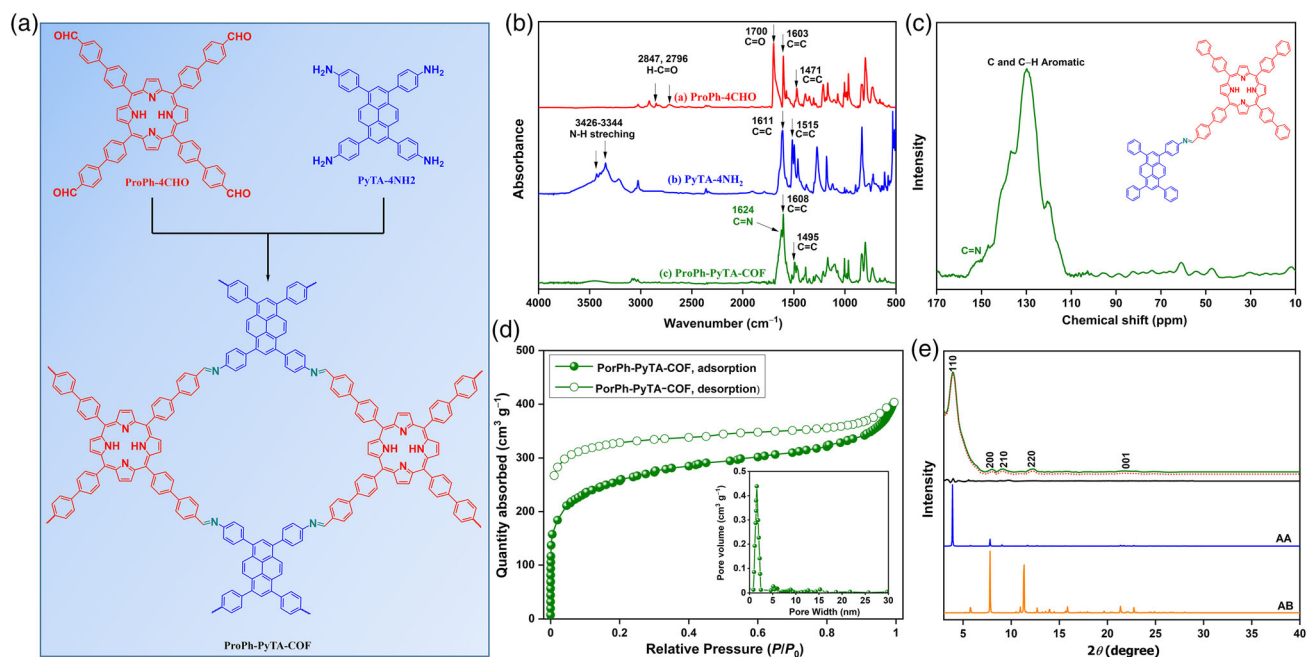

Figure 1. a) Synthesis of the π-electron-extended porphyrin/pyrene-linked covalent organic framework (ProPh-PyTA-COF). b) Fourier transform infrared (FTIR) spectra of ProPh-4CHO, PyTA-4NH₂, and the ProPh-PyTA-COF. c) Solid state ^{13}C cross-polarization (CP)/magic angle spinning (CP/MAS) nuclear magnetic resonance (NMR) spectrum of the ProPh-PyTA-COF. d) N₂ adsorption–desorption isotherm and pore size distribution (inset) of the ProPh-PyTA-COF at 77 K. e) Powder X-ray diffraction (PXRD) patterns of the ProPh-PyTA-COF: experimental (olive), simulated Pawley-refined (red), their difference (black), and simulated patterns for the 2D fully eclipsed (AA) stacking (blue) and staggered (AB) stacking (orange) succession models.

one-pot reaction of ProPh-4CHO with 4,4′,4″,4‴-pyrene-1,3,6,8-tetrayl)tetraaniline (PyTA-4NH$_2$, Figure S6 and S7, Supporting Information) at 120 °C for 72 h in a mixed solvent of n-butanol and o-dichlorobenzene (1:1) in the presence of aqueous acetic acid (6 M) as a catalyst. The formation of ProPh-PyTA-COF was confirmed by: i) the concomitant disappearance of the signals for the aldehydic C=O stretching (1700 cm^{-1}) of ProPh-4CHO and the amino N—H stretching (3426–3344 cm^{-1}) of PyTA-4NH$_2$ and ii) the appearance of a new signal at 1624 cm^{-1} in the FTIR spectrum of the ProPh-PyTA-COF, attributed to stretching of the newly formed imino C=N bonds (Figure 1b). We confirmed the chemical composition of ProPh-PyTA-COF through solid-state ^{13}C cross-polarization (CP)/magic angle spinning (MAS) NMR spectroscopy. The ^{13}C NMR spectrum of ProPh-PyTA-COF (Figure 1c) featured a distinct signal at 153.67 ppm for the carbon nuclei of the imino C=N groups, along with distinct signals in the range 146.49–111.84 ppm that we attribute to the aromatic carbon nuclei. Transmission electron microscopy (TEM) allowed us to visualize the morphology of the as-synthesized COF, revealing that the crystalline ProPh-PyTA-COF had self-assembled to generate non-regular dark and dense spheres with a layered structure and optically translucent features. In addition, the TEM images revealed an average diameter of the spherical features on the ProPh-PyTA-COF of 175 ± 30 nm (Figure S8, Supporting Information).

We performed volumetric N$_2$ adsorption/desorption experiments at 77 K to evaluate the porosity of the as-synthesized ProPh-PyTA-COF. Figure 1d reveals that the ProPh-PyTA-COF provided a type I sorption isothermal with significant N$_2$ uptake at pressures below 0.1 bar, suggesting that it was a microporous material. The specific surface area and pore volume of the ProPh-PyTA-COF, calculated from its N$_2$ adsorption data and the Brunauer–Emmett–Teller (BET) model, were 843 m^2 g^{-1} and 0.20 cm^3 g^{-1}, respectively (Table S1, Supporting Information). In addition, we used nonlocal density functional theory to derive the pore size distribution of the ProPh-PyTA-COF, revealing a unimodal porosity with a single pore size of 2.15 nm (Figure 1d, inset; Table S1, Supporting Information). We investigated the crystallinity and phase purity of our as-synthesized COF through the combination of powder X-ray diffraction (PXRD) experiments and theoretical structural simulations. The PXRD pattern of the as-synthesized ProPh-PyTA-COF featured its first and most intense peak at a low value of 2θ of 3.94°, assigned to the [110] facet (Figure 1e, olive curve). In addition, its pattern featured other minor peaks at values of 2θ of 7.96, 9.09, and 11.76°, which we ascribe to the [200], [210], and [220] facets, respectively. The hump centered at a high value of 2θ of 21.69° is attributed to the [001] facet. These clearly observed peaks in the experimental PXRD pattern confirmed the microcrystalline framework and long-range configuration of the ProPh-PyTA-COF. Furthermore, from the experimental PXRD data, the Bragg equation revealed that the center-to-center (d_{110}) and π-stacking distances between two layers of the ProPh-PyTA-COF were 2.24 nm and 4.09 Å, respectively (Table S1, Supporting Information). To provide evidence for the crystallinity of the ProPh-PyTA-COF, we used Material Studio software to simulate quasi-2D fully eclipsed (AA) stacking and staggered (AB) stacking succession models (Figure S9, Supporting Information). Interestingly, the eclipsed (AA) stacking model provided a theoretical PXRD pattern (Figure 1e, blue curve) in perfect agreement with all of the peak intensities and positions of the experimental PXRD pattern (Figure 1e, olive curve), whereas the staggered (AB) stacking model produced one (Figure 1e, orange curve) that did not, confirming the eclipsed π-stacking of the ProPh-PyTA-COF monolayers. Pawley refinement for the eclipsed (AA) stacking model of the ProPh-PyTA-COF produced a PXRD pattern (Figure 1e, red dots) matching the experimentally derived one exactly (Figure 1e, olive curve), as confirmed by the fluffy difference (Figure 1e, black curve). The triclinic unit cell of the simulated ProPh-PyTA-COF featured the following parameters: $a = 33.66$ Å; $b = 30.61$ Å; $c = 4.16$ Å; and $\alpha = \beta = \gamma = 90°$ (Table S2, Supporting Information).

ProPh-PyTA-COF possessed exceptional thermal stability, as determined through thermogravimetric analysis (TGA) under an N$_2$ atmosphere. Figure S10 and Table S3, Supporting Information, reveal that ProPh-PyTA-COF was thermally stable at temperatures up to 525 °C. After heating to 449 and 525 °C, the as-synthesized ProPh-PyTA-COF maintained approximately 95% and 90%, respectively, of its initial weight; after heating to 800 °C, the char yield was 61%. Variable-temperature PXRD analysis confirmed the thermal stability of the ProPh-PyTA-COF. Here, we evaluated the diffraction pattern constantly upon heating the ProPh-PyTA-COF at a rate of 20 °C min^{-1} under N$_2$ (Figure S11, Supporting Information). We used the normalized intensity of the [110] facet as a standard value. Figure S11, Supporting Information, reveals that the ProPh-PyTA-COF lost its crystallinity at 400 °C. The disparity between the crystallinity loss temperature and the thermal degradation temperature suggested that the ProPh-PyTA-COF first formed a disordered intermediate phase and then degraded to form volatile products at higher temperatures. We investigated the chemical and crystalline stability of the as-synthesized COF by immersing it (40 mg) at room temperature in 1,4-dioxane, N,N-dimethylformamide (DMF), acetone, and methanol (MeOH). After 72 h, we collected the COF powders by vacuum filtration, dried them at 100 °C, and finally subjected them to PXRD measurements. The intensities and locations of the signals in the PXRD patterns underwent nonsignificant changes, demonstrating the excellent chemical and crystalline stabilities of the ProPh-PyTA-COF in all of these solvents (Figure S12, Supporting Information).

2.2. Photophysical Properties of the ProPh-PyTA-COF

Because of the distinct optical and electronic properties of pyrene and porphyrin units, as well as the extended π-electron-delocalized framework resulting from the incorporation of phenyl groups, we investigated the photophysical properties of the ProPh-PyTA-COF by measuring its electronic absorption and fluorescence emissions in the dispersion state. **Figure 2**a reveals that the UV–vis absorption spectrum of the ProPh-PyTA-COF dispersed in DMF featured a characteristic narrow and intense absorption band in the wavelength region from 386 to 443 nm for the B (Soret) band and a much weaker absorption band in the range 500–700 nm for the Q band. The B(1,0) band had two components: a shoulder peak at 397 nm and a
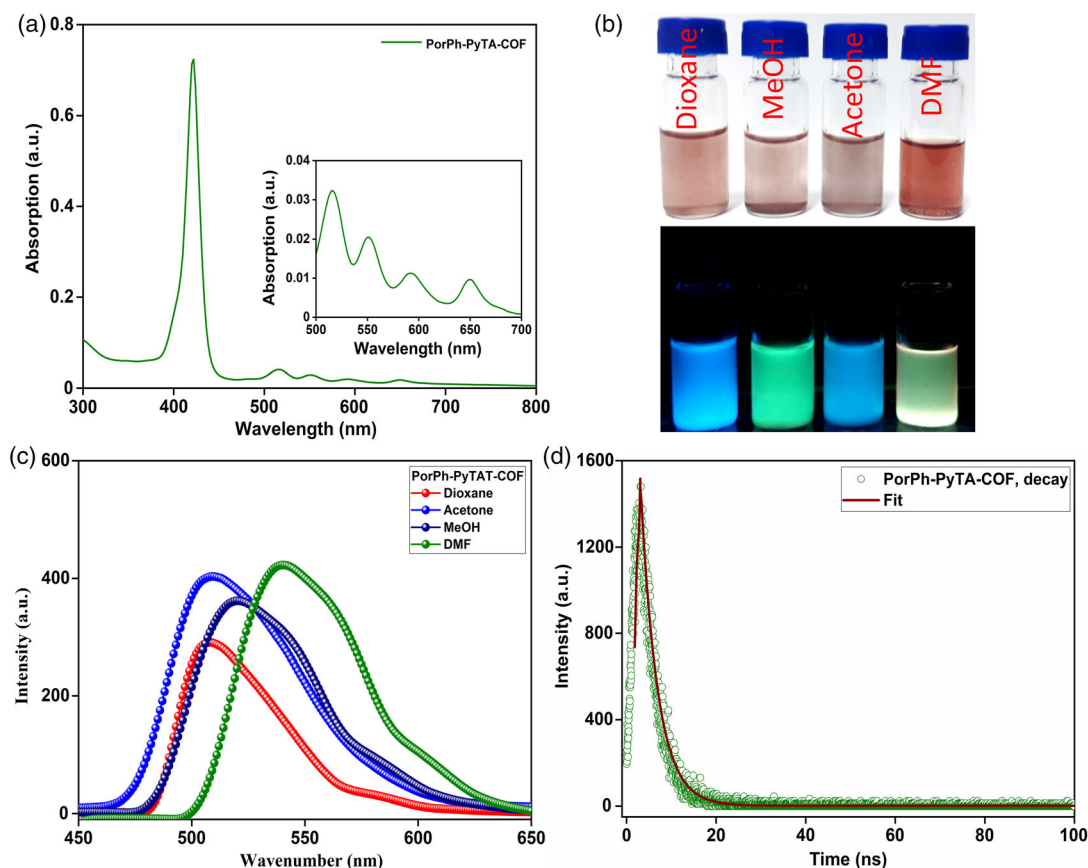
**ADVANCED
SCIENCE NEWS**

www.advancedsciencenews.com

**ADVANCED
PHOTONICS
RESEARCH**

www.adpr-journal.com

Figure 2. a) UV–vis absorption spectrum of the ProPh-PyTA-COF dispersed in *N,N*-dimethylformamide (DMF) (1 mg mL^{-1}). b) Photographic images of the ProPh-PyTA-COF dispersed in several solvents (under irradiation with a common UV light at 360 nm). c) Fluorescence emission spectra of the ProPh-PyTA-COF dispersed in several solvents (excitation at 365 nm). d) Time-resolved photoluminescence spectrum of the ProPh-PyTA-COF in DMF (excitation at 365 nm).

prominent peak at 421 nm; the Q band had four components: $Q_y(1,0)$ at 516 nm, $Q_y(0,0)$ at 550 nm, $Q_x(1,0)$ at 592 nm, and $Q_x(0,0)$ at 650 nm (Figure 2a, inset). In addition, we studied the fluorescence characteristics of the ProPh-PyTA-COF when dispersed in various solvents (Figure 2b,c). Interestingly, suspensions of the ProPh-PyTA-COF in the low-polarity solvents 1,4-dioxane and acetone exhibited strong blue fluorescence when irradiated with light from a common UV lamp (wavelength = 365 nm), while its suspensions in the high-polarity solvents MeOH and DMF exhibited strong green fluorescence, all of which were visible to the naked eye (Figure 2b). The fluorescence emission spectra of these suspensions in 1,4-dioxane, acetone, MeOH, and DMF featured fluorescence emissions with maxima centered at 507, 509, 520, and 540 nm, respectively (Figure 2c). We attribute the higher wavelengths of the fluorescence emission maxima of the ProPh-PyTA-COF in the higher-polarity solvents to the stabilization of its excited states, thereby strongly enhancing its intramolecular charge transfer processes.[41,56,57] Moreover, we used time-resolved photoluminescence spectroscopy to measure fluorescence decay lifetimes for the ProPh-PyTA-COF in 1,4-dioxane, acetone, MeOH, and DMF of 4.66, 5.57, 4.43, and 5.16 ns, respectively (Figure 2d and S13–S15, Supporting Information). Notably, these fluorescence decay

lifetimes of the ProPh-PyTA-COF are longer than those of other documented fluorescent COFs,[31,41,58] presumably because of the extended π-electron delocalization over the tetraphenylpyrene and tetraphenylporphyrin units.

2.3. Nonlinear Optical Characterization and Application in a Pulsed Laser

To characterize the optical nonlinearity and corresponding suitability for application in pulsed lasers, we prepared a COF SA sample. Here, we dispersed the COF in ethanol through ultrasonication of the COF powder for 1 h at a concentration of 4 mg mL^{-1} (**Figure 3**a). We then placed a drop of the dispersed COF solution of around 100 μL onto a 0.4 mm thick sapphire substrate. Figure 3b presents the transmission spectrum of the sample; the transmittance at 1064 nm was 64.5%. The Feng and Loh groups have previously reported the nonlinear absorptions of a series of COF samples.[11,12] The Loh group observed only reversed saturable absorption, whereas the Feng group found saturable absorption at a low intensity that turned into reversed saturable absorption at high intensity. Their reports focused on the nature of the optical nonlinearity, with less
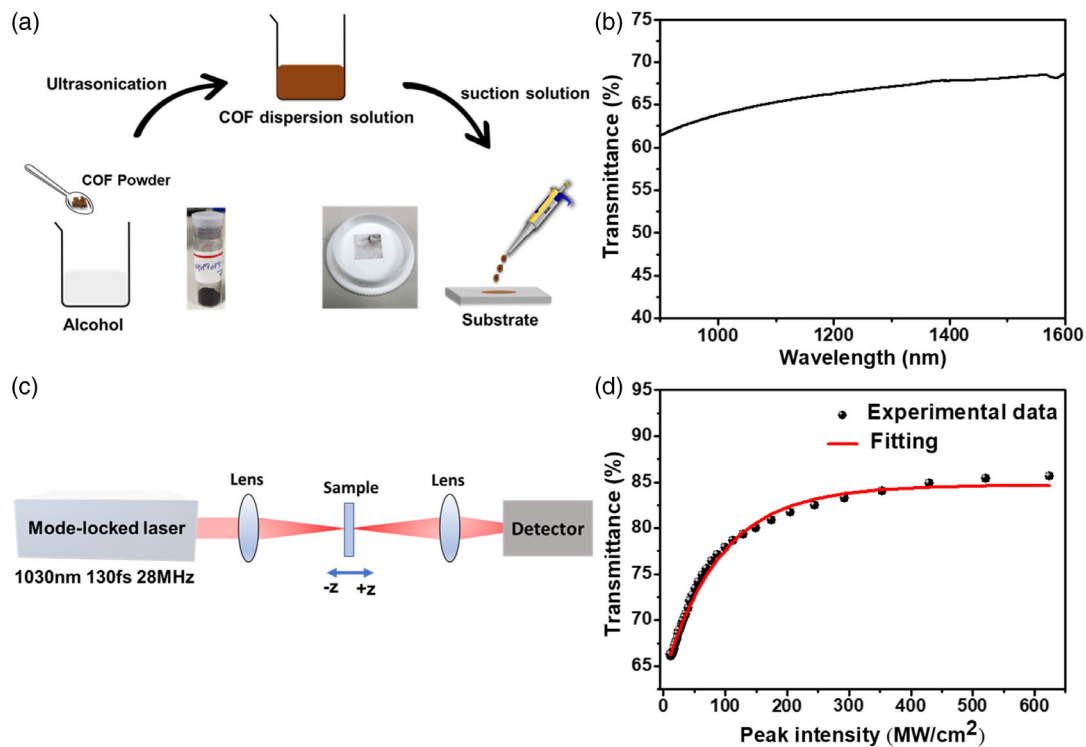
Figure 3. a) Preparation of the COF-SA sample. b) Linear transmittance of the COF plotted with respect to wavelength. c) Schematic representation of Z-scan setup. d) Corresponding nonlinear optical transmittance properties of the COF.

emphasis on, for example, measuring the saturation intensity, because they used a 532 nm Q-switched–type pulsed laser having a duration on the nanosecond scale. Typically, the pulse duration of the laser for optical nonlinearity characterization should be as short as possible to avoid the accumulation of excited photocarriers. According, for our present study, we used a mode-locked fiber laser with 130 fs pulses at 1030 nm, with a repetition rate of approximately 28 MHz, as our laser source for measurement of the saturable absorption (Figure 3c). Figure 3d presents the evolution of the transmission under various excitation intensities, determined from the open aperture z-scan data. We observe a clear dependence of the saturation with respect to the incident power. By fitting the curve with the equation

$$T(I) = 1 - \Delta T \exp\left(-\frac{I}{I_{sat}}\right) - \alpha_{ns} \quad (1)$$

where $T(I)$ is the transmittance, ΔT is the modulation depth, I is the input intensity, I_{sat} is the saturation intensity, and α_{ns} is the nonsaturable loss,[59] Figure 3d reveals that the calculated modulation depth, the saturation intensity, and the non-saturable loss of the COF were 21.2%, 92 MW cm^{-2}, and 15.5%, respectively. Notably, this study is the first, to our best knowledge, to characterize and evaluate the characteristics of the saturable absorption within a COF. In addition to confirming the optical nonlinearity in, for example, saturation, these results also indicate the potential for application of this COF in pulsed laser operation.

To demonstrate the feasibility of pulsed laser operation, we applied as-prepared COF-SA samples in an Nd:YAG laser to evaluate their Q-switching performance. We employed a V-folded resonator in the diode-pumped passively Q-switched laser (**Figure 4**a). The pump source was a fiber-coupled 808 nm diode laser having a core diameter of 0.4 mm and a numerical aperture of 0.22. The pump beam was focused into the gain medium with a waist radius of 200 μm by a 1:1 coupling optics system. The Nd:YAG crystal was cut with dimensions of $4 \times 4 \times 10$ mm^3 and had an Nd-doping concentration of 0.5%. Both sides of the Nd:YAG crystal was antireflection (AR) coated at 1064 nm; it was wrapped in indium foil and placed in a copper block, with the temperature maintained at 20 °C in a water-cooling system. The input mirror M1 was a plane mirror that was AR-coated at 808 nm and high-reflection (HR; $R > 99.8\%$)–coated at ≈1064 nm. The folding mirror M2 (radius of curvature = 100 mm) was a curved mirror having an HR coating at 1064 nm and an AR coating at 808 nm. M3, the output coupler (OC), was a plane mirror having 10% transmission at 1064 nm.

Figure 4b presents the average power with respect to the incident pump power. The threshold pump power was ≈5.6 W. We attributed the high threshold power, compared with that of ≈1 W for the COF-SAs, to the high transmission loss from the COF. Upon slightly increasing the pump power, we observed the Q-switched operation. This instance is the first pulsed laser operation using a COF as SA since Feng's SA demonstration and prediction about the application in a pulsed laser.[12] Figure 4c presents the temporal profile of the pulse at a pump power of 6.5 W; the pulse duration was 1.2 μs, corresponding to a pulse repetition rate of 94.4 kHz; the inset to Figure 4c provides the corresponding pulse trains. By finely adjusting
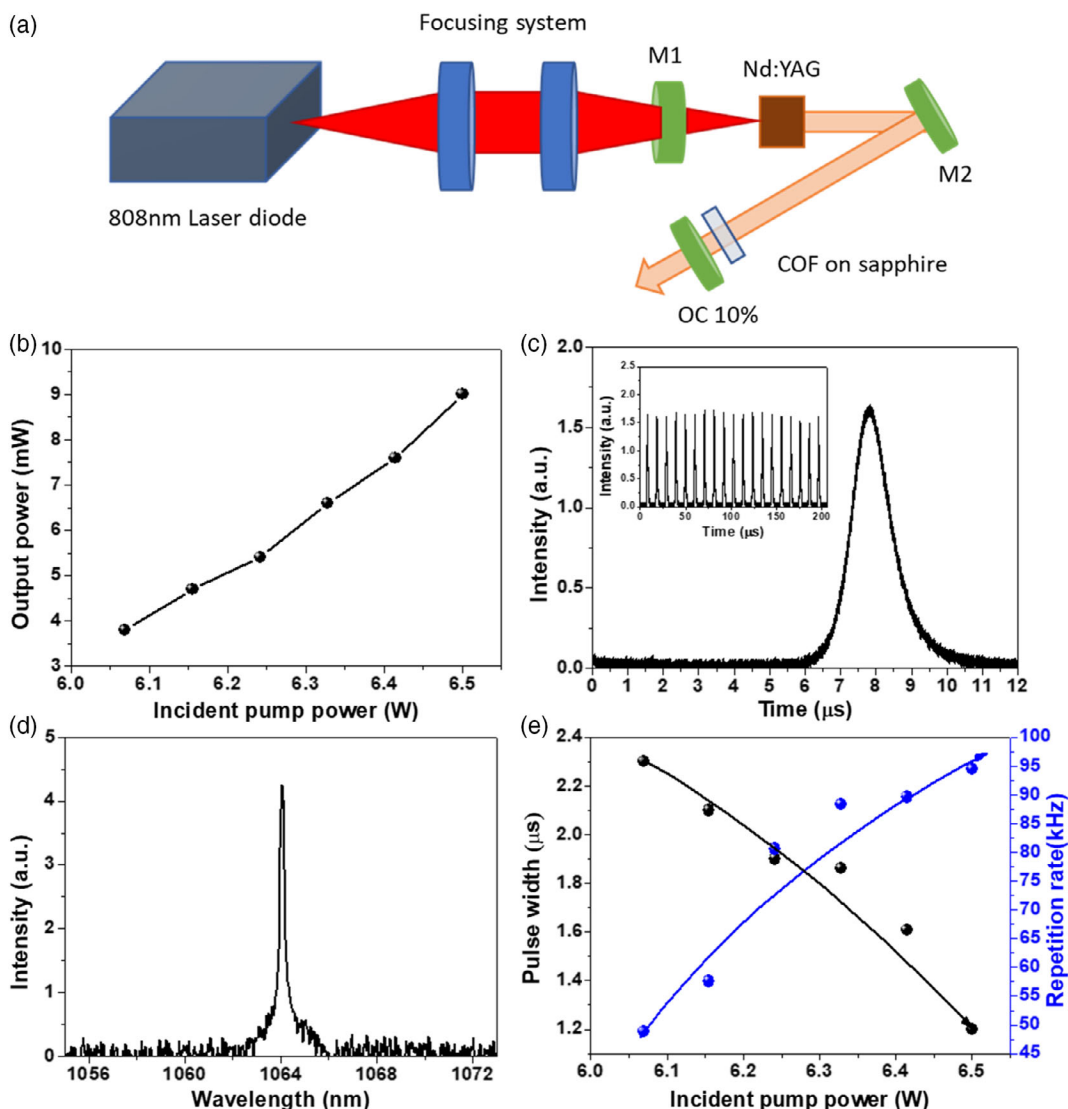
Figure 4. a) Schematic representation of the Q-switch Nd:YAG laser incorporating the COF- saturable absorber (SA) and operated at 1064 nm. b–e) Characteristics of the Q-switched laser incorporating the COF-SA. b) Output power plotted with respect to incident pump power. c) Single pulse profile; inset: pulse trains. d) Output optical spectrum. e) Pulse width and repetition rate plotted with respect to the incident pump power.

the alignment of the optics and the position of the COF-SA, we could estimate the stability through the clock amplitude jitter (CAJ), defined as the ratio of the standard deviation (σ) and mean (M) of the intensity histogram at the pulse peak intensity, using the formula[60]

$$CAJ = (\sigma/M) \times 100\% \qquad (2)$$

Accordingly, the CAJ of the pulse train was 3.8%, revealing good intensity stability. In the optical spectrum (Figure 4d), the central wavelength of the obtained Q-switched signal was 1064 nm and the 3-dB bandwidth was ≈0.4 nm. In addition, we characterized the pump power–dependent pulse duration and repetition rate. As displayed in Figure 4e, upon increasing the incident pump power from 6.07 to 6.50 W, the pulse duration shortened from 2.3 µs to a typical dependence of Q-switched

operation as pump power. Nevertheless, the laser instability increased upon further enhancing the pump power, with the pulse disappearing once the pump power exceeded 7 W. The pulsed operation and performance returned to the described conditions (Figure 4b–e) upon decreasing the pump power, suggesting that thermal damage was avoided.

The oversaturated situation of Bi_2Te_3 SAs and inside-cavity dynamics have been simulated previously using the laser rate equation.[61] As a result, we identified the phenomena observed in this present study as arising from the oversaturation of the COF-SA. To confirm this situation, we estimated the excitation intensity on the SA. Figure 4b reveals that the intensity of the SA under a pump power of 6.5 W was ≈10 kW cm^{-2}, because the spot size was ≈100 µm. This value is much lower than the measured saturation intensity of ≈92 MW cm^{-2}. The huge difference in these values suggests that the Q-switched operation might

**ADVANCED
SCIENCE NEWS**

www.advancedsciencenews.com

**ADVANCED
PHOTONICS
RESEARCH**
Open Access

www.adpr-journal.com

have arisen from the effect of another saturation intensity, other than that of 92 MW cm^{-2}. It is, however, difficult to obtain the optical nonlinear absorption at an intensity below 1000 kW cm^{-2} when using a conventional femtosecond laser. Therefore, we built a homemade 1064 nm Q-switched Nd:YAG laser for the measurement of the saturation intensity (**Figure 5**a). Here, we used Cr:YAG as the absorber for pulsing the Q-switched Nd:YAG laser. The repetition rate, pulse duration, beam spot size, and output power at a pump power of 6.6 W were 22 kHz, 40 ns, 800 μm, and 750 mW, respectively. We adjusted the excitation intensity on the COF-SA from 40 W cm^{-2} to 140 kW cm^{-2}. Figure 5b displays the evolution of the transmission upon increasing the excitation intensity. Using the same fitting formula as that in Figure 3d, the corresponding values of the modulation depth, the saturation intensity, and the non-saturable loss of the COF were 12%, 1 kW cm^{-2}, and 41%, respectively. With the same argument as that provided earlier, here the accumulation of photocarriers remained inevitable, due to the experiment being performed using a nanosecond-level excitation laser, with a lower saturation intensity even being expectable. The results suggested that there was indeed another low saturation intensity, besides that of 92 MW cm^{-2}. Consequently, the observed oversaturation was, in our case, reasonable because the intensity of 10 kW cm^{-2} was larger than the low saturation intensity.

To further realize the characteristics of nonlinear absorption, we examined the concentration effect. The concentration of the sample was defined by titrating volumes (50, 100, and 200 μL) of the dispersion, with a greater dispersion volume titrated meaning a greater amount of material covering the substrate per unit area of the substrate. By using the same experimental system as that displayed in Figure 5a, we examined the clear saturation absorption behavior under various concentrations (**Figure 6**a). The images in the inset are of the sample at various concentrations. The concentration increased upon increasing the dispersion volume. We also retrieved the characteristics of the nonlinear absorption properties from the curves; **Table 1** lists their values. Upon increasing the concentration, the saturation intensity increased from 0.7 to 1.8 kW cm^{-2} and the unsaturated absorption loss increased from 27.5 to 48.5%. This behavior suggests that the increase in absorption upon increasing the concentration led to a higher absorption loss and more power required for saturation. As a result, the decrease in the modulation depth from 15 to 7.5% upon increasing the concentration was inevitable and reasonable. In addition, to explore the effect of particle size on the nonlinear saturation absorption, we prepared fixed samples with a titration volume of 200 μL and ultrasonication times of 1, 3, and 5 h. Using the same experimental system as that in Figure 5a, we examined the clear saturation absorption behaviors under various concentrations (Figure 6b). The
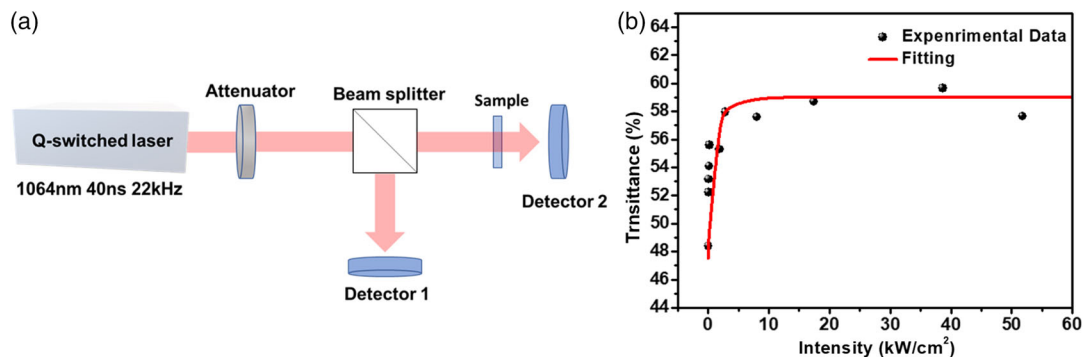

Figure 5. a) Schematic representation of the saturable absorption measurement. b) Corresponding nonlinear optical transmittance properties of the COF.
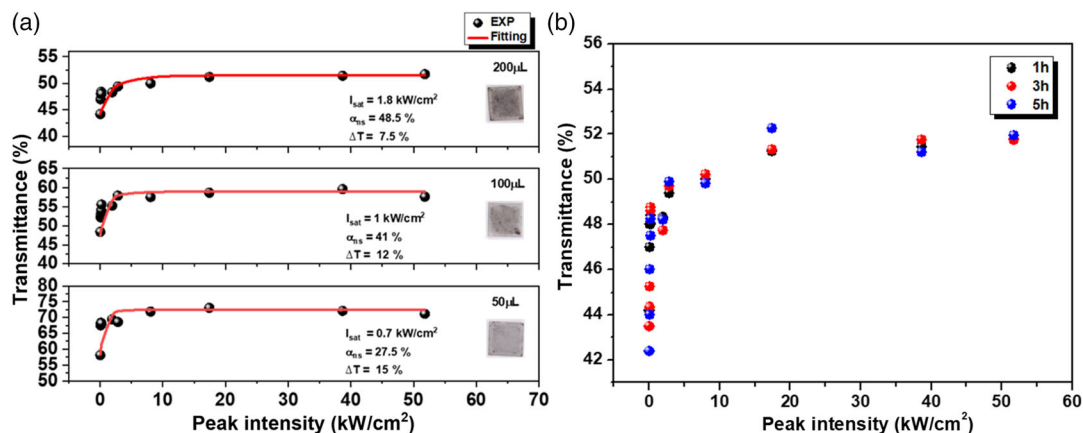

Figure 6. Nonlinear optical transmittance properties of COFs prepared a) at different concentrations and b) with different ultrasonication times.

Table 1. Saturation intensity, unsaturated absorption loss, and modulation depth of COF samples prepared at different concentrations.

	50 µL	100 µL	200 µL
I_{sat} [kW cm^{-2}]	0.7	1	1.8
α_{ns} [%]	48.5	41	27.5
ΔT [%]	15	12	7.5

measured nonlinear transmittances exhibited similar nonlinear absorption behavior for the samples that had been prepared with ultrasonication time of 1, 3, and 5 h. Thus, the ultrasonication time had only a minor effect on the particle sizes in the COF samples. Therefore, the samples exhibited similar nonlinear absorption behavior because they were prepared at the same concentration.

Organic-type nonlinear material systems have already demonstrated remarkable properties for application as optical limiters, due to the nature of the reversed saturable absorption (RSA).[62,63] Here, because our ProPh-PyTA-COF exhibited the versatile characteristics of saturable absorption, we employed it as the SA for pulsing a solid-state laser. Although the output power of the generated Q-switched laser was only a few milliwatts, we suspect that the performance could be optimized through careful cavity design.[64] In addition to the Q-switched operation, the mode-locking operation might also be possible. Indeed, Q-switched mode-locking and CW mode-locking solid-state lasers have been realized previously using low-saturation-intensity SAs.[6,65] Thus, we suspect that our COF has the potential for use in pulsed laser applications. Moreover, its versatile optical nonlinear properties open a window for engineering optical nonlinearity; such studies are in progress.

3. Conclusion

We have synthesized a novel ProPh-PyTA-COF solvothermally through the one-pot reaction of ProPh-4CHO, a new building block, and PyTA-4NH$_2$ in a mixture of n-butanol and o-dichlorobenzene (1:1). The resultant ProPh-PyTA-COF exhibited high crystallinity, a very large BET surface area (843 m^2 g^{-1}), extreme thermal stability (up to 525 °C), and ultrahigh chemical stability in various organic solvents as well as acidic and basic aqueous solutions. Because of the distinct optical and electronic properties of both its pyrene and porphyrin units, as well as the extended π-electron-delocalized framework formed by incorporating additional phenyl groups, the ProPh-PyTA-COF exhibited distinct optical properties, including versatile optical nonlinear properties and two saturation absorptions. Meanwhile, we prepared the first example of a Q-switched solid-state laser incorporating a COF (ProPh-PyTA-COF) as the SA. Our study not only demonstrates the possibility of using saturation absorption to pulse a solid-state laser but also opens up a new window for developing optical nonlinearity through the engineering of π-bond delocalization.

Supporting Information

Supporting Information is available from the Wiley Online Library or from the author.

Conflict of Interest

The authors declare no conflict of interest.

Data Availability Statement

Research data are not shared.

[1] T. Maiman, *Nature* **1960**, *187*, 493.
[2] A. Weiner, *Ultrafast Optics*, Wiley, Hoboken, NJ **2013**.
[3] B. Zhang, J. Liu, C. Wang, K. Yang, C. Lee, H. Zhang, J. He, *Laser Photonics Rev.* **2019**, *14*, 1900240.
[4] U. Keller, K. Weingarten, F. Kartner, D. Kopf, B. Braun, I. Jung, R. Fluck, C. Honninger, N. Matuschek, J. Aus der Au, *IEEE J. Sel. Top. Quantum Electron.* **1996**, *2*, 435.
[5] H. Zhang, D. Tang, R. Knize, L. Zhao, Q. Bao, K. Loh, *Appl. Phys. Lett.* **2010**, *96*, 111112.
[6] Y. Wang, J. He, C. Lee, W. Sung, X. Su, Y. Zhao, B. Zhang, C. Wu, G. He, Y. Lin, H. Liu, *IEEE Photonics J.* **2018**, *10*, 1.
[7] X. Sun, H. Nie, J. He, R. Zhao, X. Su, Y. Wang, B. Zhang, R. Wang, K. Yang, *Opt. Express* **2017**, *25*, 20025.
[8] G. Zhao, J. Hou, Y. Wu, J. He, X. Hao, *Adv. Opt. Mater.* **2015**, *3*, 937.
[9] J. Jhon, J. Koo, B. Anasori, M. Seo, J. Lee, Y. Gogotsi, Y. Jhon, *Adv. Mater.* **2017**, *29*, 1702496.
[10] X. Jiang, L. Zhang, S. Liu, Y. Zhang, Z. He, W. Li, F. Zhang, Y. Shi, W. Lü, Y. Li, Q. Wen, J. Li, J. Feng, S. Ruan, Y. Zeng, X. Zhu, Y. Lu, H. Zhang, *Adv. Opt. Mater.* **2018**, *6*, 1800561.
[11] X. Li, Q. Gao, J. Aneesh, H. Xu, Z. Chen, W. Tang, C. Liu, X. Shi, K. Adarsh, Y. Lu, K. Loh, *Chem. Mater.* **2018**, *30*, 5743.
[12] B. Biswal, S. Valligatla, M. Wang, T. Banerjee, N. Saad, B. Mariserla, N. Chandrasekhar, D. Becker, M. Addicoat, I. Senkovska, R. Berger, D. Rao, S. Kaskel, X. Feng, *Angew. Chem., Int. Ed.* **2019**, *58*, 6896.
[13] C. S. Diercks, O. M. Yaghi, *Science* **2017**, *355*, 923.
[14] A. P. Cote, A. I. Benin, N. W. Ockwig, M. O'Keeffe, A. J. Matzger, O. M. Yaghi, *Science* **2005**, *310*, 1166.
[15] S. Ding, W. Wang, *Chem. Soc. Rev.* **2013**, *42*, 548.
[16] N. Huang, P. Wang, D. Jiang, *Nat. Rev. Mater.* **2016**, *1*, 16068.
[17] S. Kandambeth, K. Dey, R. Banerjee, *J. Am. Chem. Soc.* **2019**, *141*, 1807.

[18] A. F. M. EL-Mahdy, M. B. Zakaria, H. X. Wang, T. Chen, Y. Yamauchi, S. W. Kuo, *J. Mater. Chem. A* **2020**, *8*, 25148.

[19] A. F. M. El-Mahdy, C. H. Kuo, A. Alshehri, C. Young, Y. Yamauchi, J. Kim, S. W. Kuo, *J. Mater. Chem. A* **2018**, *6*, 19532.

[20] B. P. Biswal, H. A. Vignolo-González, T. Banerjee, L. Grunenberg, G. Savasci, K. Gottschling, B. V. Lotsch, *J. Am. Chem. Soc.* **2019**, *141*, 11082.

[21] W. Zhao, L. Xia, X. Liu, *CrystEngComm* **2018**, *20*, 1613.

[22] H. R. Abuzeid, A. F. M. EL-Mahdy, S. W. Kuo, *Micropor. Mesopor. Mat.* **2020**, *300*, 110151.

[23] K. Y. Lin, A. F. M. El-Mahdy, *Mater. Chem. Phys.* **2022**, *281*, 125850.

[24] A. F. M. El-Mahdy, C. Young, J. Kim, J. You, Y. Yamauchi, S. W. Kuo, *ACS Appl. Mater. Interfaces* **2019**, *11*, 9343.

[25] E. Jin, M. Asada, Q. Xu, S. Dalapati, M. Addicoat, M. A. Brady, H. Xu, T. Nakamura, T. Heine, Q. Chen, *Science* **2017**, *357*, 673.

[26] L. Zhang, S. Wang, Y. Zhou, C. Wang, X. Z. Zhang, H. Deng, *Angew. Chem., Int. Ed.* **2019**, *131*, 14351.

[27] A. M. Elewa, A. F. M. EL-Mahdy, A. E. Hassan, Z. Wen, J. Jayakumar, T. L. Lee, L. Y. Ting, I. M. A. Mekhemer, T. F. Huang, M. H. Elsayed, C. L. Chang, W. C. Lin, H. H. Chou, *J. Mater. Chem. A* **2022**, *10*, 12378.

[28] H. R. Abuzeid, A. F. M. EL-Mahdy, M. M. M. Ahmed, S. W. Kuo, *Polym. Chem.* **2019**, *10*, 6010.

[29] S. Wang, Q. Wang, P. Shao, Y. Han, X. Gao, L. Ma, S. Yuan, X. Ma, J. Zhou, X. Feng, *J. Am. Chem. Soc.* **2017**, *139*, 4258.

[30] W. R. Cui, C. R. Zhang, W. Jiang, F. F. Li, R. P. Liang, J. Liu, J. D. Qiu, *Nat. Commun* **2020**, *11*, 436.

[31] A. F. M. EL-Mahdy, A. M. Elewa, S. W. Huang, H. H. Chou, S. W. Kuo, *Adv. Opt. Mater.* **2020**, *8*, 2000641.

[32] X. Li, Q. Gao, J. Wang, Y. Chen, Z. H. Chen, H. S. Xu, W. Tang, K. Leng, G. H. Ning, J. Wu, Q. H. Xu, S. Y. Queck, Y. Lu, K. P. Loh, *Nat. Commun.* **2018**, *9*, 2335.

[33] M. Wang, M. Hu, J. Liu, C. Guo, D. Peng, Q. Jia, L. He, Z. Zhang, M. Du, *Biosens. Bioelectron.* **2019**, *132*, 8.

[34] N. Huang, L. Zhai, H. Xu, D. Jiang, *J. Am. Chem. Soc.* **2017**, *139*, 2428.

[35] Y. Li, C.-X. Yang, X.-P. Yan, *Chem. Commun.* **2017**, *53*, 2511.

[36] S. Jin, X. Ding, X. Feng, M. Supur, K. Furukawa, S. Takahashi, M. Addicoat, E. M. El-Khouly, T. Nakamura, S. Irle, S. Fukuzumi, A. Nagai, D. Jiang, *Angew. Chem., Int. Ed.* **2013**, *52*, 2017.

[37] S. Jin, K. Furukawa, M. Addicoat, L. Chen, S. Takahashi, S. Irle, T. Nakamura, D. Jiang, *Chem. Sci.* **2013**, *4*, 4505.

[38] J. Guo, Y. Xu, S. Jin, L. Chen, T. Kaji, Y. Honsho, M. Addicoat, J. Kim, A. Saeki, H. Ihee, S. Seki, S. Irle, M. Hiramoto, J. Gao, D. Jiang, *Nat. Commun.* **2013**, *4*, 2736.

[39] M. Dogru, M. Handloser, F. Auras, T. Kunz, D. Medina, A. Hartschuh, P. Knochel, T. Bein, *Angew. Chem., Int. Ed.* **2013**, *52*, 2920.

[40] D. D. Medina, J. M. Rotter, Y. Hu, M. Dogru, V. Werner, F. Auras, J. T. Markiewicz, P. Knochel, T. Bein, *J. Am. Chem. Soc.* **2015**, *137*, 1016.

[41] A. F. M. EL-Mahdy, M. Y. Lai, S. W. Kuo, *J. Mater. Chem. C* **2020**, *8*, 9520.

[42] L. R. Ahmed, A. F. M. EL-Mahdy, C. T. Pan, S. W. Kuo, *Mater. Adv.* **2021**, *2*, 4617.

[43] W. Li, X. Huang, T. Zeng, Y. A. Liu, W. Hu, H. Yang, Y. B. Zhang, K. Wen, *Angew. Chem., Int. Ed.* **2121**, *133*, 1897.

[44] G. de la Torre, P. Vazquez, F. Agullo-Lopez, T. Torres, *Chem. Rev.* **2004**, *104*, 3723.

[45] K. McEwan, K. Lewis, G. Y. Yang, L. L. Chng, Y. W. Lee, W. P. Lau, K. S. Lai, *Adv. Funct. Mater.* **2003**, *13*, 863.

[46] C. Gu, H. Zhang, P. You, Q. Zhang, G. Luo, Q. Shen, Z. Wang, J. Hu, *Nano Lett.* **2019**, *19*, 9095.

[47] K. Kurlekar, A. Anjali, S. Sonalin, P. M. Imran, S. Nagarajan, *ACS Appl. Electron. Mater.* **2020**, *2*, 3402.

[48] J. L. Shi, R. Chen, H. Hao, C. Wang, X. Lang, *Angew. Chem., Int. Ed.* **2020**, *59*, 9088.

[49] V. Piradi, G. Zhang, T. Li, M. Zhang, Q. Peng, X. Zhan, X. Zhu, *ACS Appl. Mater. Interfaces* **2020**, *12*, 41506.

[50] S. Kandambeth, D. B. Shinde, M. K. Panda, B. Lukose, T. Heine, R. Banerjee, *Angew. Chem., Int. Ed.* **2013**, *52*, 13052.

[51] X. Xu, S. Wang, Y. Yue, N. Huang, *ACS Appl. Mater. Interfaces* **2020**, *12*, 37427.

[52] R. Chen, Y. Wang, Y. Ma, A. Mal, X. Y. Gao, L. Gao, L. Qiao, X. B. Li, L. Z. Wu, C. Wang, *Nat. Commun.* **2021**, *12*, 1354.

[53] M. Chen, H. Li, C. Liu, J. Liu, Y. Feng, A. G. Wee, B. Zhang, *Coord. Chem. Rev.* **2021**, *435*, 213778.

[54] J. Guo, D. Jiang, *ACS Cent. Sci.* **2020**, *6*, 869.

[55] S. Bhunia, S. K. Das, R. Jana, S. C. Peter, S. Bhattacharya, M. Addicoat, A. Bhaumik, A. Pradhan, *ACS Appl. Mater. Interfaces* **2017**, *9*, 23843.

[56] A. S. Klymchenko, *Acc. Chem. Res.* **2017**, *50*, 366.

[57] K. Li, J. Cui, Z. Yang, Y. Huo, W. Duan, S. Gong, Z. Liu, *Dalton Trans.* **2018**, *47*, 15002.

[58] M. Kou, W. Liu, Y. Wang, J. Huang, Y. Chen, Y. Zhou, Y. Chen, M. Ma, K. Lei, H. Xie, P. K. Wong, *Appl. Catal. B: Environ.* **2021**, *291*, 120146.

[59] S. Chen, C. Zhao, Y. Li, H. Huang, S. Lu, H. Zhang, S. Wen, *Opt. Mater. Express* **2014**, *4*, 587.

[60] J. Qiao, S. Zhao, K. Yang, W. Song, W. Qiao, C. Wu, J. Zhao, G. Li, D. Li, T. Li, H. Liu, C. Lee, *Photonics Res.* **2018**, *6*, 314.

[61] Y. Lin, W. Song, P. Lee, Y. Wang, H. Zhang, C. Lee, *J. Phys. Commun.* **2018**, *2*, 125007.

[62] D. Li, Z. Gu, J. Zhang, *Chem. Sci.* **2020**, *11*, 1935.

[63] D. Li, Q. Li, Z. Gu, J. Zhang, *Nano Lett.* **2021**, *21*, 10012.

[64] Y. Lin, P. Lee, J. Xu, C. Wu, C. Chou, C. Tu, M. Chou, C. Lee, *IEEE Photonics J.* **2016**, *8*, 1502710.

[65] J. Xu, Y. Sun, J. He, Y. Wang, Z. Zhu, Z. You, J. Li, M. Chou, C. Lee, C. Tu, *Sci. Rep.* **2015**, *5*, 14856.